# Access to Mars from Earth-Moon Libration Point Orbits: Manifold and Direct Options

Masaki Kakoi*, Kathleen C. Howell

*School of Aeronautics and Astronautics, Purdue University, West Lafayette, IN, USA*

David Folta

*NASA Goddard Space Flight Center, Greenbelt, MD, USA*

## Abstract

This investigation is focused specifically on transfers from Earth-Moon $L_1/L_2$ libration point orbits to Mars. Initially, the analysis is based in the circular restricted three-body problem to utilize the framework of the invariant manifolds. Various departure scenarios are compared, including arcs that leverage manifolds associated with the Sun-Earth $L_2$ orbits as well as non-manifold trajectories. For the manifold options, ballistic transfers from Earth-Moon $L_2$ libration point orbits to Sun-Earth $L_1/L_2$ halo orbits are first computed. This autonomous procedure applies to both departure and arrival between the Earth-Moon and Sun-Earth systems. Departure times in the lunar cycle, amplitudes and types of libration point orbits, manifold selection, and the orientation/location of the surface of section all contribute to produce a variety of options. As the destination planet, the ephemeris position for Mars is employed throughout the analysis. The complete transfer is transitioned to the ephemeris model after the initial design phase. Results for multiple departure/arrival scenarios are compared.

*Keywords:*
Multi-body dynamics, Circular restricted three-body problem, Invariant manifolds, Libration point orbits, System-to-system transfer, Mars

*Corresponding author, 701 W. Stadium Ave., West Lafayette, IN 47907-2045, USA, 1-765-494-5813, 1-765-494-0307 (Fax)

*Email addresses:* kakoi@purdue.edu (Masaki Kakoi), howell@purdue.edu (Kathleen C. Howell), david.c.folta@nasa.gov (David Folta)

## 1. INTRODUCTION

The far side of the lunar surface has held global interest for many years. One of the challenges in exploring the far side of the Moon is communications from/to the Earth. Multiple satellites are required to maintain a continuous link if a communications architecture relies only on lunar-centered orbits. Farquhar and Breakwell suggested an unusual three-body approach in response to this challenge in 1971 [1]. This concept requires only one satellite by exploiting the characteristics of three-dimensional halo orbits in the vicinity of the Earth-Moon $L_2$ ( EM$L_2$) libration point. Unfortunately, this plan was never implemented due to a shortening of the Apollo program. However, interest in the exploration of the far side of the Moon has recently increased, particularly in the aftermath of the successful Artemis mission [2]. In addition, a new exploration strategy has recently emerged, that is, possibly establishing a space station in an EM$L_1/L_2$ orbit and leveraging this station as a hub for the exploration of the asteroids and Mars [3].

The potential of an EM$L_1/L_2$ hub for further exploration is yet to be investigated extensively. To examine the feasibility, mission designers require an improved understanding of the dynamics that influence a transfer trajectory from EM$L_1/L_2$ libration point orbits to possible destination objects, and the capability to produce such trajectories via a reasonably straightforward and efficient design process. Analysis concerning possible trajectories from EM$L_1/L_2$ orbits to Mars is explored by applying dynamical relationships available as a result of formulating the problem in terms of multiple three-body gravitational environments.

## 2. PREVIOUS CONTRIBUTIONS

Within the last decade, interest in a mission design approach that leverages the knowledge of dynamical systems theory (DST) has increased steadily amongst scholars and trajectory designers. Howell et al. examined the application of DST within a mission design process in the late 1990's [4]. The knowledge was actually applied to design the GENESIS mission trajectory, launched in 2001 [5, 6]. GENESIS was the first spacecraft for which the concept of invariant manifolds was directly applied to develop the actual path of the vehicle [7]. The successful return of the GENESIS spacecraft demonstrated that DST can be exploited for actual trajectory design in multi-body

environments. Scientific missions such as MAP and WIND also relied upon three-body dynamics for their successful trajectory designs in the same time frame [8, 9].

As the result of a set of successful missions, interest in DST applications to trajectory design has increased and researchers have expanded their investigation to exploit DST and better understand the dynamics in the more complex four-body systems which consist of three gravitational bodies and one spacecraft. In the early 2000's, Gómez et al. introduced a methodology to design transfer trajectories between two circular restricted three-body systems by exploiting invariant manifold structures [10, 11]. They modeled a four-body system by blending two CR3BPs. The investigations into such system-to-system transfers was originally based on a Jupiter-moon system as well as spacecraft moving in the Sun-Earth-Moon neighborhood [12, 13, 14]. But, Gómez et al. demonstrated the potential exploitation of the CR3BP as a modeling tool to investigate four-body systems. Parker and Lo employed the coplanar model to design three-dimensional trajectories from Low Earth Orbits (LEO) to Earth-Moon $L_2$ halo orbits [15]. In addition, Parker also applied DST as a design tool to develop transfer strategies from LEO to a broader range of EM halo orbits [16, 17, 18]. The investigation in the Sun-Earth-Moon system eventually was extended to transfers between libration point orbits in the Sun-Earth and Earth-Moon systems. Howell and Kakoi introduced a model with an inclination between the Earth-Moon and the Sun-Earth systems to design transfers between Earth-Moon $L_2$ halo orbits and Sun-Earth $L_2$ halo orbits [19]. Canalias and Masdemont extended the investigation to transfers between quasi-periodic Lissajous orbits in different systems, i.e., Earth-Moon and Sun-Earth [20]. In addition, transfer trajectory design methods between Earth-Moon and Sun-Earth systems have been investigated using various other strategies as well [21, 16, 18, 22, 23].

Dynamical systems theory has also been suggested as a design tool for interplanetary trajectory design [24, 25]. However, since manifolds associated with the Sun-Earth libration point orbits do not intersect manifolds associated with other Sun-planet systems, such as Sun-Mars or Sun-Jupiter systems, different techniques have been developed for interplanetary transfer arcs. Alonso and Topputo et al. investigated techniques to link non-intersecting manifolds with an intermediate high energy trajectory arc [26, 27, 28]. Nakamiya et al. analyzed maneuver strategies at perigee and periareion for Earth-to-Mars transfers [29, 30]. As alternatives to the high energy arcs, low-thrust arcs have also been investigated for transfers between the two

systems [31, 32, 33, 22, 34]

The past investigations on the system-to-system transfer design strategies have successfully contributed numerous design techniques and insight in the four-body regime. However, trajectory design techniques from the Earth-Moon libration point orbits to interplanetary destinations warrants further examination.

## 3. SYSTEM MODEL

One of the most important trajectory design tools is a reasonable model that represents the physical system to a certain level of accuracy and offers the desired system characteristics. But the model must also be sufficiently simple such that mission designers can readily analyze the dynamics and interactions between various trajectory arcs. The circular restricted three-body problem offers both the complexity and the well-known manifold structures to represent the actual motion that can be exploited.

### *3.1. Circular Restricted Three-Body Problem*

A schematic of the fundamental definitions in the circular restricted three-body problem (CR3BP) appears in Figure 1. Primary bodies, $P_1$ and $P_2$, rotate about their mutual barycenter at a constant distance and with a constant angular velocity. The masses of $P_1$ and $P_2$ are defined as $m_1$ and $m_2$. A massless body, $P_3$, moves under the gravitational influence of the primary bodies. An inertial frame is defined by a set of three orthogonal vectors $[\hat{X},\hat{Y},\hat{Z}]$. The unit vector $\hat{Z}$ aligns with the angular momentum vector for the planar motion of the primary bodies. The unit vector $\hat{X}$ is defined on the plane of motion of the primaries. Then, the unit vector $\hat{Y}$ completes the right-handed triad. A set of three orthogonal vectors $[\hat{x},\hat{y},\hat{z}]$ defines a rotating frame in which the equations of motion are derived. The unit vector $\hat{x}$ is defined in the direction from $P_1$ toward $P_2$, and the unit vector $\hat{z}$ is aligned with $\hat{Z}$. Then, the unit vector $\hat{y}$ completes the right-handed triad. Therefore, when the angle $\theta$ in Figure 1 is 0°, $[\hat{X},\hat{Y},\hat{Z}]$ and $[\hat{x},\hat{y},\hat{z}]$ are identically aligned. The nondimensional mass ratio $\mu$ is defined as $\mu = \frac{m_2}{m_1+m_2}$. Distances are nondimensionalized utilizing the distance between primaries as the characteristic length, $r^*$. The nondimensional location of $P_3$ with respect to the barycenter in the rotating frame is denoted as $\bar{r}$, and the nondimensional vector is expressed as $\bar{r} = x\hat{x} + y\hat{y} + z\hat{z}$. Also, the location of $P_3$ with

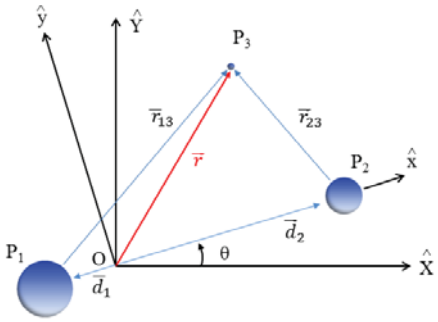


Figure 1: Formulation of the Circular Restricted Three-Body Problem

respect to $P_1$ and $P_2$ is denoted as $\bar{r}_{13}$ and $\bar{r}_{23}$, respectively. Time is nondimensionalized by the mean motion of primaries, $n = \sqrt{\frac{G(m_1+m_2)}{r^{*3}}}$, where $G$ is the universal gravitational constant.

The differential equations governing the CR3BP do admit a constant of the motion. The value of this Jacobi constant is defined as follows,

$$C_J = -(\dot{x} + \dot{y} + \dot{z}) + x^2 + y^2 + 2(\frac{1-\mu}{r_{13}} + \frac{\mu}{r_{23}}). \tag{1}$$

Dots indicate derivatives with respect to the nondimensional time, and $r_{13}$ and $r_{23}$ are magnitudes of $\bar{r}_{13}$ and $\bar{r}_{23}$, respectively. The Jacobi constant, $C_J$, is the only integral of motion and indicates the energy level of $P_3$ in its orbit as computed in the CR3BP.

### *3.2. Blending CR3BPs*

The circular restricted three-body problem has been successfully demonstrated as a powerful design tool to provide insight into the actual motion of a body in space such as a spacecraft or a comet [35, 36]. Of course, the number and types of gravitational bodies for the design of some specific trajectory vary depending on the spacecraft destination, and the CR3BP itself may not be sufficient to model the appropriate dynamical regime. Hence, the capability to model a system with more than two gravitational bodies is essential. One approach to model such a system that has been previously explored is a blending of CR3BPs. For example, a four-body system such as Sun-Earth-Moon can be modeled by overlapping Sun-Earth and Earth-Moon systems at the common body, Earth. This technique can incorporate the difference in the orientation of the fundamental orbital planes of the two

systems to enhance the level of accuracy. In Figure 2, the location of the Moon is defined relative to the other bodies in the system. The rotating frame corresponding to the Sun-Earth system is defined as a set of three orthogonal unit vectors $[\hat{a}_1, \hat{a}_2, \hat{a}_3]$. The Sun is located in the direction corresponding to $-\hat{a_1}$. Another set of three orthogonal unit vectors $[\hat{b}_1, \hat{b}_2, \hat{b}_3]$ reflects the rotating frame of the Earth-Moon system, and the orientation of $[\hat{b}_1, \hat{b}_2, \hat{b}_3]$ with respect to $[\hat{a}_1, \hat{a}_2, \hat{a}_3]$ is defined by a Euler angle sequence, i.e., body-two 3-1-3. The first angle $\alpha$ defines the orientation of the line of nodes with respect to $\hat{a}_1$. The second angle $i$ denotes the inclination of the lunar orbit plane with respect to the Earth orbit. The third angle $\beta$ identifies the lunar location in the orbital plane relative to the line of nodes, i.e., the ascending node.

A similar model formulation is possible to design interplanetary trajectories by blending a Sun-Earth system and a Sun-planet system. For example, to design a trajectory from Earth to Mars, Sun-Earth and Sun-Mars systems are overlapped at the common body, i.e., the Sun. In this case, the inclination of Mars' orbit is generally neglected since the inclination relative to the ecliptic plane is 1.51°, relatively small compared to the lunar orbit inclination, 5.09° [37]. Then, the location of Mars with respect to the Sun-Earth rotating frame is defined by only one angle. This assumption simplifies the model and is generally adequate for a corrections process. However, the Mars' orbit is more elliptic than the Earth's or the Moon's orbit. The eccentricity of the Mars' orbit is 0.0934 compared to 0.0167 and 0.0549 of the Earth's orbit and the Moon's orbit, respectively [37]. Therefore, the exploitation of a circular restricted model for the Sun-Mars system reduces the level of accuracy. However, the goal is an effective initial guess for the higher-fidelity model, i.e., one that can be transitioned while retaining similar trajectory characteristics. This investigation examines the viability of such a model.

### *3.3. Dynamical Model for Transfers to Mars*

To achieve a higher level of accuracy in the construction of a preliminary path, the ephemeris Mars locations are incorporated into the system model. Two options are available for this Mars' orbit model. The first option incorporates the Mars' gravitational force. The gravitational force from Mars is computed in an inertial frame, based on the location of a spacecraft as well as the epoch. Thus, the exploitation of the CR3BP is not trivial in this formulation. An alternative strategy is the incorporation of only the state information for the ephemeris locations of Mars. In this model, the

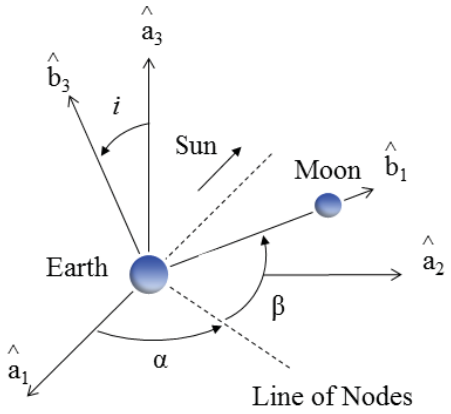


Figure 2: Angle Definitions in the Three-Dimensional Model: Euler angle sequence body-two 3-1-3

Mars data is transformed into the Sun-Earth rotating frame and the trajectory design process is executed in the Sun-Earth system. This option allows incorporation of Mars' actual position into the CR3BP.

## 4. MULTIPLE SHOOTING

Trajectory design requires the capability to link different types of arcs, including both two-body and three-body arcs, to meet mission requirements. The same type of corrections process is also employed to transition to a model of different fidelity or add new forces to an existing model. One possible strategy to accomplish such a task is a multiple shooting method [38]. Such a numerical corrections scheme has been demonstrated to be useful in trajectory design [39, 40]. A multiple shooting schematic is illustrated in Figure 3. The black dots represent 6-D states estimated to be on a desirable path, that is, to serve as an initial guess. The states are denoted $\bar{x}_i$ where the subscript $i$ is an index. Each $\bar{x}_i$ is comprised of position components as well as velocity components, e.g., $\bar{x}_1 = [r_{x1}, r_{y1}, r_{z1}, v_{x1}, v_{y1}, v_{z1}]$. Propagating a state, $\bar{x}_i$, over time, $t_i$, by means of function $\bar{f}$ yields the trajectory represented by a solid arc in the figure. As an initial guess, the state $\bar{x}_i$ does not, in fact, reach the desired state $\bar{x}_{i+1}$ after the propagation. The actual final state along each arc is denoted by $\bar{f}(\bar{x}_i, t_i)$, and it is defined by position components, $r^f_{xi}, r^f_{yi}, r^f_{zi}$ and velocity components, $v^f_{xi}, v^f_{yi}, v^f_{zi}$ as $\bar{f}(\bar{x}_i, t_i) = [r^f_{xi}, r^f_{yi}, r^f_{zi}, v^f_{xi}, v^f_{yi}, v^f_{zi}]$. The superscript $f$ indicates the final state along arc $i$. If arcs are not linked, as in the figure, final states from the

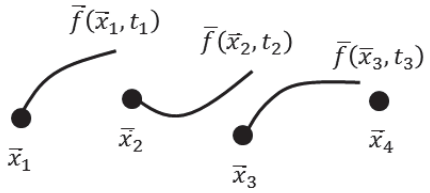


Figure 3: Illustration of Multiple Shooting

propagation, $\bar{f}(\bar{x}_i, t_i)$, and the following initial states $\bar{x}_{i+1}$ are modified to achieve a continuous trajectory. To achieve a continuous path, various types of corrections strategies could be applied. From among many options, a free-variable/constraint implementation of the corrections process is employed. This corrections process is detailed in Pavlak [41]. A free variable vector, $\bar{X}$, and a constraint vector, $\bar{F}$, are defined as follows,

$$\bar{X} = [\bar{x}_1,\ t_1,\ \bar{x}_2,\ t_2,\ \bar{x}_3,\ t_3]^T, \tag{2}$$

$$\bar{F}(\bar{X}) = \left[\bar{x}_2 - \bar{f}(\bar{x}_1, t_1),\ \bar{x}_3 - \bar{f}(\bar{x}_2, t_2),\ \bar{x}_4 - \bar{f}(\bar{x}_3, t_3)\right]^T = \bar{0}, \tag{3}$$

where $\bar{X}$ is a column vector of free variables and $\bar{F}$ is a column vector of equality constraints. The superscript $T$ indicates a transpose. Then, these constraints are achieved numerically by the iterative application of a vector Newton's method. Generally, the number of free variables is larger than the number of constraints. The $DF(\bar{X}_j)$ matrix is not expected to be invertible. Thus, the standard Newton update is modified employing a pseudo-inverse of $DF(\bar{X}_j)$, such that

$$\bar{X}_{j+1} = \bar{X}_j - DF(\bar{X}_j)^T[DF(\bar{X}_j) \cdot DF(\bar{X}_j)^T]^{-1}\bar{F}(\bar{X}_j). \tag{4}$$

where $\bar{X}_j$ is a free variable vector at the $j^{th}$ iteration and $DF(\bar{X}_j)$ is the Jacobian matrix. The Jacobian matrix is constructed as partial derivatives of the constraint vector with respect to the free variable vector evaluated at the $j^{th}$ iteration. This formulation is generally quick to implement and efficient.

In a multiple shooting process, introducing maneuvers to link multiple arcs increases flexibility. A maneuver option is simply formulated by omitting velocity components from the specified constraint. For example, define an alternative constraint vector for $\bar{f}(\bar{x}_2, t_2)$. To allow a maneuver at $\bar{f}(\bar{x}_2, t_2)$,

the new vector is formulated as follows,

$$\bar{F}_2 = [r_{x3},\ r_{y3},\ r_{z3}]^T - [r^f_{x2},\ r^f_{y2},\ r^f_{z2}]^T = \bar{0}. \tag{5}$$

An additional scalar constraint to limit the velocity difference by the magnitude of the maneuver, $\Delta V$, between $\bar{x}_3$ and $\bar{f}(\bar{x}_2, t_2)$ is incorporated as the following,

$$F_{\Delta V} = (v_{x3} - v^f_{x2})^2 + (v_{y3} - v^f_{y2})^2 + (v_{z3} - v^f_{z2})^2 - \Delta V^2 = 0. \tag{6}$$

The constraint $F_{\Delta V}$ actually specifies the allowable $\Delta V$ level. Thus, to improve the application of the constraint $F_{\Delta V}$ to introduce flexibility, an inequality constraint is a better alternative. The inequality is formulated as an equality constraint by introducing a slack variable, $\eta$, and the new formulation is written,

$$\begin{aligned} F_{\Delta V} &= (v_{x3} - v^f_{x2})^2 + (v_{y3} - v^f_{y2})^2 + (v_{z3} - v^f_{z2})^2 \\ &\quad -(\Delta V - \eta^2)^2 = 0. \end{aligned} \tag{7}$$

The slack variable $\eta$ is squared such that $\Delta V$ - $\eta^2$ is always smaller than or equal to $\Delta V$. Then, the final formulation with a scalar $\Delta V$ constraint at $\bar{x}_3$ is the following,

$$\bar{X} = [\bar{x}_1,\ t_1,\ \bar{x}_2,\ t_2,\ \bar{x}_3,\ t_3,\ \eta]^T, \tag{8}$$

$$\bar{F}(\bar{X}) = \left[\bar{F}_1,\ \bar{F}_2,\ \bar{F}_3,\ F_{\Delta V}\right]^T = \bar{0}, \tag{9}$$

where

$$\bar{F}_1 = \bar{x}_2 - f(\bar{x}_1, t_1), \tag{10}$$

$$\bar{F}_2 = [r_{x3},\ r_{y3},\ r_{z3}] - [r^f_{x2},\ r^f_{y2},\ r^f_{z2}], \tag{11}$$

$$\bar{F}_3 = \bar{x}_4 - f(\bar{x}_3, t_3), \tag{12}$$

$$\begin{aligned} F_{\Delta V} &= ((v_{x3} - v^f_{x2})^2 + (v_{y3} - v^f_{y2})^2 + (v_{z3} - v^f_{z2})^2 \\ &\quad -(\Delta V - \eta^2)^2. \end{aligned} \tag{13}$$

The maximum maneuver size, $\Delta V$, and an initial guess for $\eta$ are required to solve for $\bar{F} = \bar{0}$. The initial guess for $\eta$ is selected such that the scalar constraint is satisfied, i.e., $F_{\Delta V} = 0$.

## 5. MANEUVER-FREE TRANSFERS BETWEEN EARTH-MOON AND SUN-EARTH SYSTEMS

One possible scenario for a transfer from a three-dimensional Earth-Moon (EM) halo orbit to the planet Mars is the exploitation of unstable Sun-Earth (SE) manifolds. However, to utilize this option, it is necessary to transfer from an EM halo orbit to a manifold trajectory associated with a SE halo orbit. Even though different techniques for such transfers have been investigated by linking manifolds associated with EM halo orbits to those corresponding to SE halo orbits, it is still challenging to compute maneuver-free transfers between the Earth-Moon system and the Sun-Earth system. Thus, it is crucial to establish a general process to construct maneuver-free transfers for exploiting SE manifolds as a platform for departure to Mars.

### *5.1. Hyperplane and Reference Frame*

A hyperplane is useful for computing halo-to-halo spacecraft transfers. In Figure 4, the $x$-$y$ projections of a hyperplane (black line) and Earth-Moon manifold trajectories, in red, are plotted in Sun-Earth coordinates. The location of the hyperplane is defined by an angle $\psi$, and it is measured from the Sun-Earth $x$-axis in the counter-clockwise direction. Thus, $\psi$ is negative in Figure 4. State vectors corresponding to both Earth-Moon and Sun-Earth manifolds are then projected onto the hyperplane as the paths pass through the plane; this projected information offers valuable insight for the computation of maneuver-free transfer paths. To visualize the projected information as phase plots, a new reference frame is defined on the hyperplane by a set of orthogonal unit vectors $[\hat{x}_{ref}, \hat{y}_{ref}, \hat{z}_{ref}]$. The intersection between the Sun-Earth $x$-$y$ plane and the hyperplane defines $\hat{x}_{ref}$, as viewed in Figure 4. The direction of $\hat{x}_{ref}$ is defined so that $\hat{x}_{ref}$ becomes identical with $\hat{x}$ in the Sun-Earth system when $\psi$ is equal to zero degrees. The unit vector $\hat{z}_{ref}$ is identical to the Sun-Earth $\hat{z}$ axis. The cross product between $\hat{z}_{ref}$ and $\hat{x}_{ref}$ defines $\hat{y}_{ref}$. Position and velocity components expressed in terms of the hyperplane reference frame are represented as $[x_{ref}, y_{ref}, z_{ref}, \dot{x}_{ref}, \dot{y}_{ref}, \dot{z}_{ref}]$. Phase plots represented in this reference frame are exploited to discover the lunar location and the appropriate Sun-Earth libration point orbit for a maneuver-free transfer from an Earth-Moon halo orbit with a specified amplitude. The size of a periodic halo orbit is distinguished by the $z$ amplitude, $Az$, of the orbit which is measured from the $x$-axis to the largest excursion of the orbit in the $\hat{z}$ direction, as viewed in Figure 5.

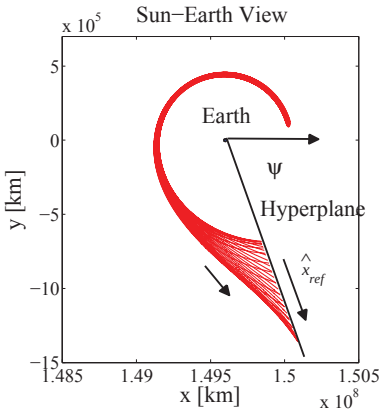


Figure 4: Definition of $\psi$: It is measured from the SE $x$-axis in the counter-clockwise direction (The default value for $\psi$ is negative and $\psi < 0$ in the figure).

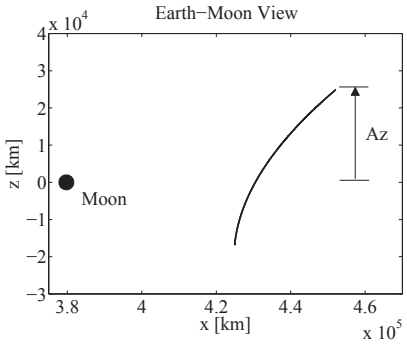


Figure 5: Definition of $Az$: An Earth-Moon halo orbit projected onto the Earth-Moon $x$-$z$ plane

### *5.2. Phase Plots to Establish Orientation of Earth-Moon System*

To achieve a maneuver-free transfer, the appropriate combination of all variables must be determined including $\alpha$, $\beta$, $\psi$, EM$Az$, and SE$Az$. Although a challenging task, the procedure to compute the appropriate values is simplified by exploiting the phase plots created by the projection of the appropriate states on the hyperplane that is, essentially, a two-dimensional space.

The location of a hyperplane is a key element in obtaining useful phase plots. Generally, the desirable range for the value of the hyperplane angle, $\psi$, is between $-85°$ and $-70°$ to achieve maneuver-free transfers from EM$L_2$ halo orbits to SE$L_2$ halo orbits. Although the range varies as a function of

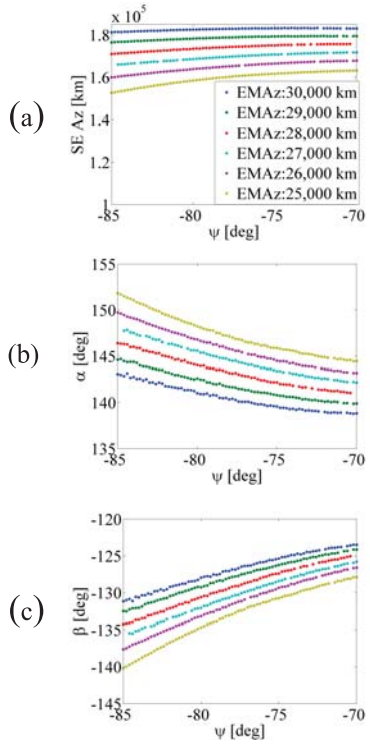


Figure 6: Conditions for Maneuver-Free Transfers from EM halo orbits to SE halo orbits

the size of the departure halo orbit as well as the direction of the transfers, examination of a specific transfer type, such as EM$L_2$-to-SE$L_2$ transfers, supplies useful information which is applicable to various transfer alternatives. In Figure 6, conditions for maneuver-free transfers are displayed. In Figure 6(a), the required combinations of SE$Az$ and EM$Az$ at specified values of $\psi$ appear. Values for SE$Az$ and $\psi$ are then estimated for a specific EM$Az$ value from the figure. Plots in Figures 6(b)-(c) offer appropriate estimates for $\alpha$ and $\beta$ values, respectively, corresponding to the specific combination of EM$Az$ and $\psi$.

Various types of phase plots associated with the hyperplane are actually available. However, this investigation demonstrates that three phase plots are sufficient to compute a transfer. The three phase plots selected for analysis are: $(i)$ $\dot{x}_{ref}$ vs $x_{ref}$, $(ii)$ $z_{ref}$ vs $x_{ref}$, and $(iii)$ $\dot{z}_{ref}$ vs $z_{ref}$. Some examples appear in Figure 7. In each phase plot, Earth-Moon and Sun-Earth manifolds appear as closed curves due to the 'tube-like' struc-

ture of the manifolds. Since the Jacobi constant value indicates the energy level for a trajectory in the CR3BP, the Jacobi constant values corresponding to the intersecting Earth-Moon and Sun-Earth manifolds must be equal to achieve a maneuver-free transfer. In the Earth-Moon rotating frame, the Jacobi constant value corresponding to any point along the manifold is equal to the value of the associated Earth-Moon halo orbit. However, the value is no longer constant after the states along the manifold are transformed into the Sun-Earth rotating frame. Thus, the Jacobi constant value varies along the EM manifold curve in the phase plots, which are represented in the Sun-Earth system. A black circle on each phase plot in Figure 7 indicates the location, along the EM manifold, that corresponds to a Jacobi constant value that is equal to the value along the entire set of trajectories that define the Sun-Earth manifold. The hyperplane guarantees the $y_{ref}$ intersection by definition. The intersection of the two curves in the $\dot{x}_{ref}$ vs $x_{ref}$ phase plot guarantees the existence of an EM manifold trajectory with a corresponding match in $\dot{x}_{ref}$ and $x_{ref}$ values along the SE manifold. Therefore, if the same intersecting EM manifold trajectory possesses an intersection in the other two phase plots, all states, except $\dot{y}_{ref}$, are equal in value. Thus, it is necessary to introduce an additional relationship related to $\dot{y}_{ref}$. However, rather than introducing another phase plot, Jacobi constant values are utilized in this process to 'match' the last component, i.e., $\dot{y}_{ref}$. In Figure 7, the black circle clearly indicates the direction in which the red curve should be shifted in each phase plot. For example, in Figure 7(a), it is clear that the red curve should be shifted to the left to move the black circle towards the blue curve.

### *5.3. Guidelines*

For a given halo amplitude EM$Az$, the orientation of the Earth-Moon system determines the red curves in the phase plots, e.g., in Figure 7, for a fixed value of $\psi$. Thus, changing the values of $\alpha$ and $\beta$ shifts the red curves; adjusting $\alpha$ and $\beta$ essentially modifies the location of the Moon in its orbit. The blue curves remain the same on the fixed hyperplane for a given value of SE$Az$. The plots in Figure 8 demonstrate that various shifts of the red curve in each phase plot slide the black circle toward the blue curve. The process to achieve the intersection in all three phase plots is automated. The guidelines for the process are summarized as follows:

- Plots (b) and (c) in Figure 6 correlate the values of $\alpha$ and $\beta$ that are necessary to achieve a maneuver-free transfer for a desired set of EM$Az$

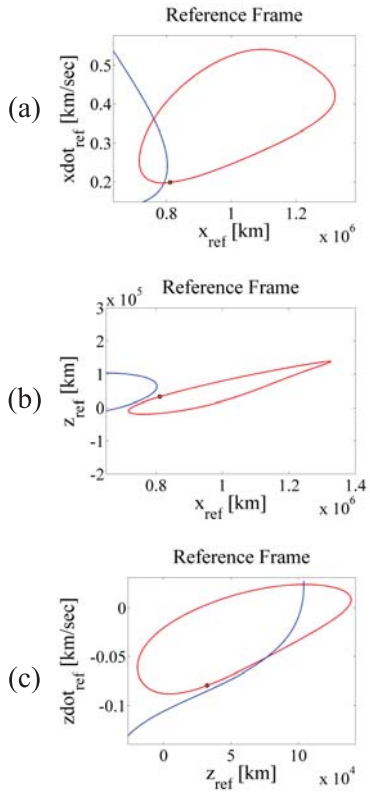


Figure 7: Selected Phase Plots at Hyperplane: Blue and red curves are projections of stable SE and unstable EM manifold trajectories, respectively, in the SE view. Black circles highlight the EM manifold trajectory with the SE Jacobi constant value.

and $\psi$ values in this model. These results are useful to estimate the initial values for the design process.

- For the $\dot{x}_{ref}$ vs $x_{ref}$ phase plot in Figures 7 and 8, either $\alpha$ or $\beta$ can be adjusted to shift the black circle closer to the blue curve.

- In the $z_{ref}$ vs $x_{ref}$ phase plot in Figure 7(b), most likely, the black circle does not intersect with the blue curve, even after an intersection is achieved in the $\dot{x}_{ref}$ vs $x_{ref}$ phase plot. Thus, the black circle must be shifted to intersect with the blue curve by modifying the values of $\alpha$ and $\beta$. However, such an update also changes the $\dot{x}_{ref}$ vs $x_{ref}$ phase plot. Maintaining the summation of $\alpha$ and $\beta$ as a constant reduces the effect on the $\dot{x}_{ref}$ vs $x_{ref}$ phase plot in Figures 7(a) and 8(a). For

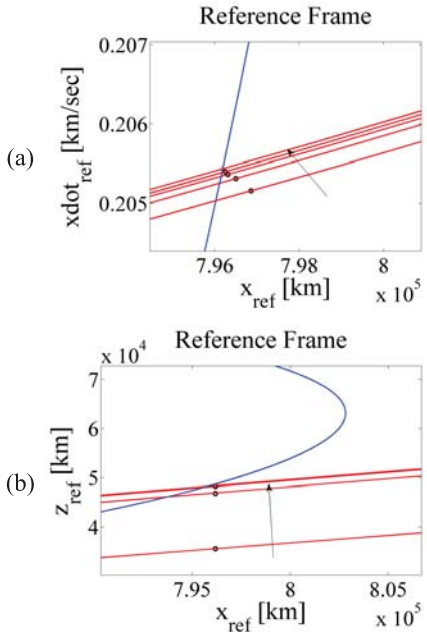


Figure 8: Phase Plots as Trajectory Design Tools: Blue and red curves are projections of stable SE and unstable EM manifolds. Black circles highlight the location, along the EM manifold, with the SE Jacobi constant value. The arrow indicates the direction in which the red curve shifts.

example, if $\alpha$ is shifted by $1^\circ$, $\beta$ is altered by $-1^\circ$. Physically, the adjustments in $\alpha$ and $\beta$ change the location of the Moon by month and day, respectively. Updating $\beta$ in the opposite direction reduces the shift of the state along the manifold. However, the shift reduction is small in the $z$-component.

- To achieve the intersection in the $\dot{z}_{ref}$ vs $z_{ref}$ phase plot, the Sun-Earth amplitude ($Az$ value) is adjusted. Since this adjustment affects other phase plots, both $\dot{x}_{ref}$ vs $x_{ref}$ and $z_{ref}$ vs $x_{ref}$ phase plots are then re-evaluated.

Sample phase plots that are produced at the completion of the process appear in Figure 9. The black circle intersects the blue curve in all the phase plots and a maneuver-free transfer is constructed. In Figure 10, the black trajectory is computed from the state identified in the final phase plots. This trajectory links an unstable Earth-Moon manifold trajectory and approaches a Sun-Earth halo orbit. In this figure, the trajectory shifts from a

Table 1: Sample Results for EM-SE Transfers

| Type | EM$Az$ [km] | SE$Az$ [km] | $\psi$ [deg] | $\alpha$ [deg] | $i$ [deg] | $\beta$ [deg] |
|---|---|---|---|---|---|---|
| EM$L_2$ to SE$L_2$ | 25,000 | 163,200 | -70 | 144.47 | 5 | -127.88 |
| EM$L_2$ to SE$L_2$ | 26,000 | 167,900 | -70 | 143.20 | 5 | -126.60 |
| EM$L_2$ to SE$L_2$ | 27,000 | 171,800 | -70 | 142.17 | 5 | -125.80 |
| SE$L_2$ to EM$L_2$ | 25,000 | 163,900 | 70 | 35.89 | 5 | -52.68 |
| EM$L_2$ to SE$L_1$ | 25,000 | 162,600 | 110 | -37.38 | 5 | -124.68 |
| SE$L_1$ to EM$L_2$ | 25,000 | 163,000 | -110 | -142.46 | 5 | -55.59 |

stable Sun-Earth manifold to an unstable Sun-Earth manifold such that the path actually departs the SE halo orbit. It can be numerically corrected to remain on the SE halo orbit if desired.

These guidelines are sufficiently general to be applied to different transfer types including Earth-Moon $L_2$ halo orbits to/from Sun-Earth $L_2$ halo orbits and Earth-Moon $L_2$ halo orbits to/from Sun-Earth $L_1$ halo orbits. Sample results are summarized in Table 1. The first three examples in the table represent the same transfer type, Earth-Moon $L_2$ to Sun-Earth $L_2$, but incorporating different Earth-Moon $Az$ values. As the Earth-Moon $Az$ value changes, the Sun-Earth $Az$ value and phase angles shift. However, since the changes are small, these values of the SE$Az$ amplitude and phase angles yield a reasonable initial guess for different Earth-Moon $Az$ amplitudes. The fourth example in Table 1 is a transfer in the opposite direction, i.e., from Sun-Earth $L_2$ to Earth-Moon $L_2$; such a path reflects a return to the Earth-Moon neighborhood. When the transfer direction is reversed, the $\psi$ value reverses sign from $-70^\circ$ to $70^\circ$ while the $Az$ value is barely affected. The SE$L_2$-to-EM$L_2$ transfer is plotted in Figure 11(a). The transfer is nearly symmetric as compared to the EM$L_2$-to-SE$L_2$ transfer, in Figure 10, across the Sun-Earth $x$-axis. Similarly, the EM$L_2$-to-SE$L_1$ and SE$L_1$-to-EM$L_2$ transfers in Figures 11(b)-(c), respectively, are symmetric to each other across the Sun-Earth $x$-axis.

## 6. TRANSFER SCENARIOS

Multiple departure scenarios are examined in this investigation. Since each scenario possesses its own advantages and disadvantages, one scenario may be better suited for certain mission requirements, and/or different destinations.

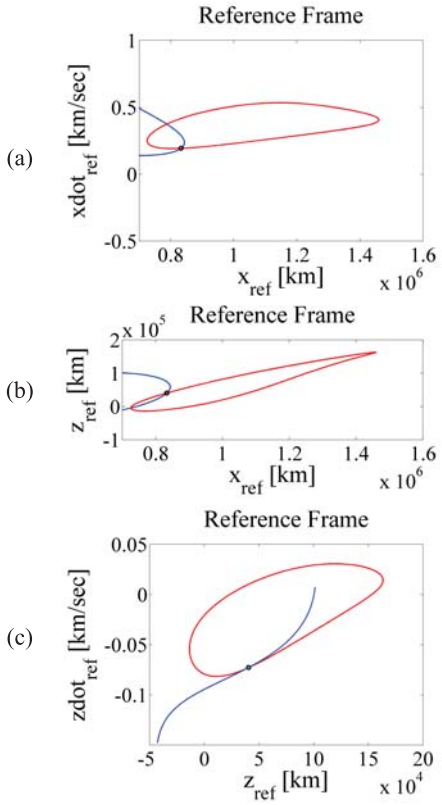


Figure 9: Phase Plots for Earth-Moon $L_2$ Halo Orbit to Sun-Earth $L_2$ Halo Orbit Transfer

### *6.1. Transfers via Sun-Earth Manifold*

The first type of scenario to produce a Mars transfer utilizes a halo-to-halo transfer. This transfer scenario does not offer much flexibility in the departure date since the combination of $\alpha$ and $\beta$ values to compute a halo-to-halo transfer between selected EM$Az$ and SE$Az$ is limited as is apparent in Figure 6. Based on the $\alpha$ and $\beta$ values, multiple possible departure dates can be identified. However, the location of Mars at the arrival time limits the possible date ranges. Although this process is automated, the guidelines for computing successful transfers under this scenario are:

- Possible departure dates are identified by comparing the angle combination ($\alpha$, $i$, and $\beta$) with the phase angles corresponding to the ephemeris Moon's orbital position. Multiple departure dates are available based on the angle information.

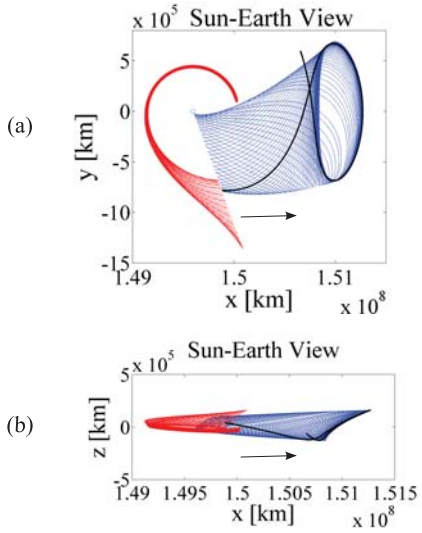


Figure 10: Transfer from Earth-Moon $L_2$ Halo orbit to Sun-Earth $L_2$ Halo Orbit: EM$Az$ = 25,000 km, SE$Az$ = 163,200 km, $\psi$ = -70 deg. A trajectory propagated from the phase plots' conditions is in black. Arrows indicate the direction of flow.

- Time-of-flight to Mars from a Sun-Earth manifold trajectory is initially estimated by computing a Hohmann transfer arc. Based on possible departure dates and the total time-of-flight, the appropriate locations of Mars at various arrival times are identified. Under the assumptions in this analysis, it becomes apparent that most of the possible departure dates are not feasible due to Mars' location at arrival.

- Based on an estimated feasible arrival date, the actual ephemeris location of Mars is obtained from the Mars database. Then, an osculating semi-major axis for the Mars' orbit at the arrival time is computed. Re-computing the Hohmann transfer trajectory to Mars with the new semi-major axis improves the $\Delta V$ estimation.

- Previous contributers have exploited unstable Sun-Earth manifolds in the exterior region for departure arcs. However, in this scenario, stable Sun-Earth manifolds are exploited for the departure arcs, as viewed in Figure 12, since the time-of-flight becomes significantly shorter. In addition, consistent with a two-body analysis, the energy change, or the $\Delta V$ value, is slightly improved by the exploitation of stable manifolds.

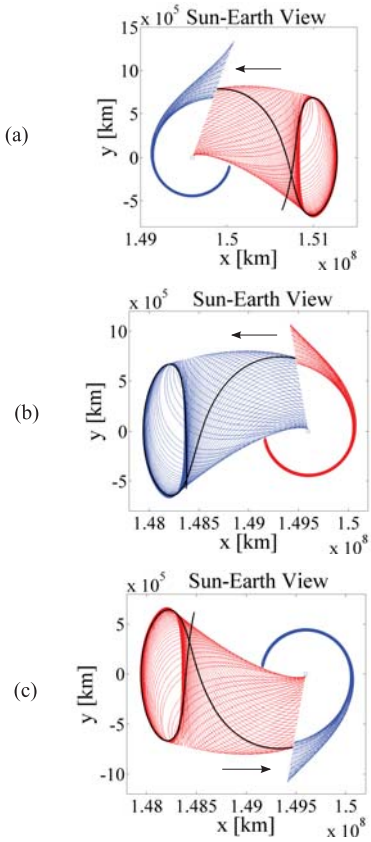


Figure 11: Various Transfers between an Earth-Moon $L_2$ Halo orbit and Sun-Earth $L_1/L_2$ Halo Orbit: EM$Az$ = 25,000 km: unstable manifold trajectories in red, stable manifold trajectories in blue. Arrows indicate the direction of flow.

Also, the maneuver magnitude, i.e., $\Delta V$, tends to be smaller when applied along the stable SE manifold near $x$-axis.

- Two maneuvers are applied by implementing a multiple shooting scheme. The first maneuver is applied to depart a Sun-Earth stable manifold path. The location of the second maneuver is free to shift along the path as required.

In Figure 12, a transfer trajectory to Mars is constructed by modification of the conditions from the first case in Table 1. The ephemeris Mars' orbit is displayed in green in Figures 12(c)-(d). Earth-Moon manifold trajectories are in red in Figures 12(a)-(b) and Sun-Earth manifold trajectories are plotted

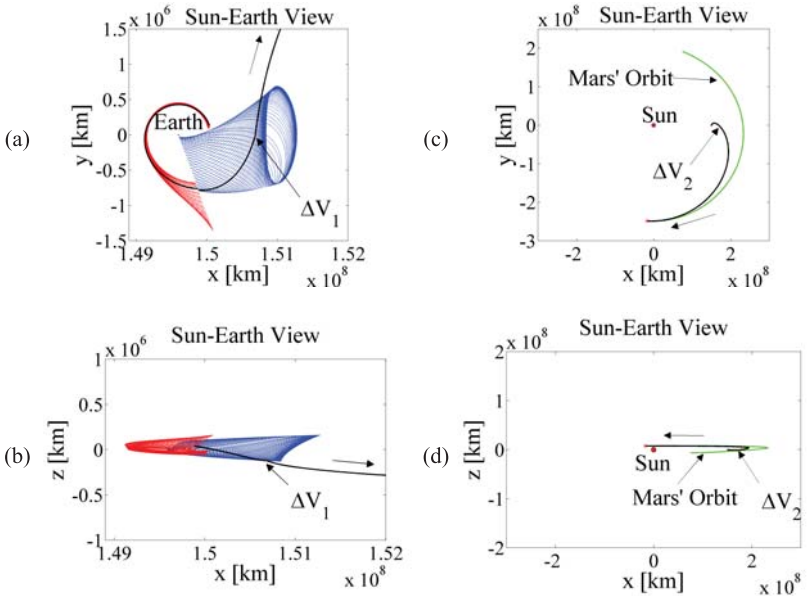


Figure 12: Transfer from Earth-Moon $L_2$ to Mars via Sun-Earth Manifold: EM$Az$ = 25,000 km, SE$Az$ = 163,200 km, $\psi$ = -70 deg

Table 2: Sun-Earth Manifold Transfer

| Case | Departure Date | Total TOF [day] | $\Delta V$ [km/sec] |
|---|---|---|---|
| One Maneuver | June 16, 2022 | 277 | 3.869 |
| Two Maneuvers | June 16, 2022 | 350 | 3.495 |

in blue. Results for a departure date of June 16, 2022 appear in Table 2. The results demonstrate that the application of two maneuvers allows a reduction of the total $\Delta V$ from 3.869 km/sec to 3.495 km/sec. Two locations where maneuvers occur are indicated in Figures 12(b)-(c). Since an unstable EM manifold trajectory is exploited to leave the EM halo orbit, no significant $\Delta V$ is required. However, the increase in the time-of-flight from 277 days to 350 days is notable. In this example, the $\Delta V$ is reduced as the arrival approach to Mars becomes more tangential. The value of $\Delta V$ is higher than the estimated value from the planar Hohmann transfer which is 2.8 km/sec from the same location along the manifold. The balance of the total $\Delta V$ is mostly due to targeting the $z$-component of the ephemeris Mars position. The ephemeris Mars' orbit is described with an the average inclination of 1.85° [37]. However, this small inclination has a significant impact on the $\Delta V$ value.

*6.2. Transfers via Earth-Moon Manifold*

For the second scenario, an Earth-Moon manifold is again exploited to depart an Earth-Moon $L_2$ halo orbit. However, in this scenario, rather than shifting to a Sun-Earth manifold path, the trajectory continues on the Earth-Moon manifold and returns to the vicinity of the Earth to gain energy via an Earth "gravity assist" to depart the vicinity of the Earth. Not surprisingly, this scenario offers more flexibility in departure dates compared to the first example. To effectively accomplish a gravity assist and gain the promised flexibility, certain conditions must be satisfied. One of the conditions is a relatively close pass distance; another is a perigee location in the fourth quadrant relative to the Sun-Earth frame. Earth-Moon manifold paths as viewed in the Sun-Earth rotating frame are plotted in red in Figure 13. The hyperplane orientation is fixed at $\psi = -95°$; the angles $\alpha$ and $\beta$ are each equal to 0°. To observe the flow of the trajectories along the manifold passing through the hyperplane, the states at the hyperplane crossing are integrated forward in the Sun-Earth system. The integrated trajectories appear in black in the figure. Since the behavior of these trajectories is complex, it is extremely challenging to predict the variations in the path as a function of the variations in $\alpha$, $\beta$, and $\psi$. Therefore, thousands of combinations of $\alpha$, $\beta$, and $\psi$ are examined and reflected in the final strategy.

The location of perigee associated with each combination of $\alpha$, $\beta$, and $\psi$ must be identified. Thus, the perigee location is defined by an angle $\kappa$ as displayed in Figure 14. The angle $\kappa$ is measured from the Sun-Earth $x$-axis in the counter-clockwise direction. The plot in Figure 15 demonstrates the perigee conditions corresponding to the Earth-Moon manifold trajectories for hyperplane orientations in terms of $\psi$ from 0° to 360°. The desired conditions recur periodically and offer possibilities for potentially promising flyby conditions. The guidelines to design transfers from the Earth-Moon $L_2$ orbit to Mars, through Earth-Moon manifold trajectories and incorporating a close Earth pass, are summarized as follows:

- The perigee condition for the trajectory integrated in the Sun-Earth system must be verified. Generally, Earth passage distances that equal thousands of kilometers or even tens of thousands of kilometers are adequate initial guesses to be employed in a multiple shooting scheme. A maneuver is applied at the apogee location along the manifold trajectory to achieve the desired perigee condition as demonstrated in Figure 16. If the perigee condition is not desirable, there are three options to

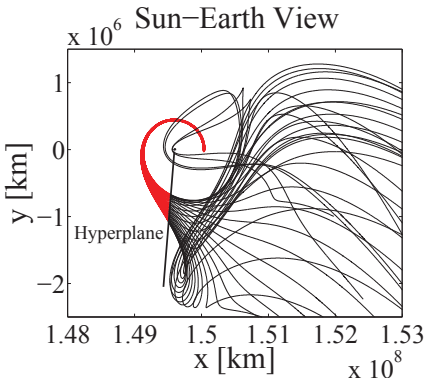


Figure 13: Earth-Moon Manifolds in Sun-Earth Frame: $\psi = -95°$, $\alpha = \beta = 0°$

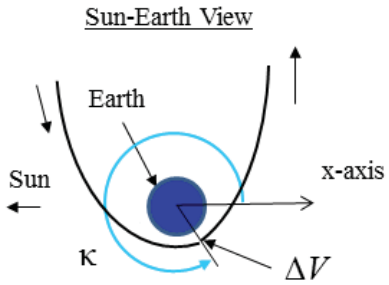


Figure 14: Definition of $\kappa$: Perigee location

improve the perigee guess. The first option is the selection of a different manifold path. The second option involves the selection of alternate values for the $\alpha$ and $\beta$ combination. Changing two angles in an open search for desirable perigee conditions without any guidance is clearly not a good design strategy. However, by linking the ephemeris lunar location to the system model, the departure date automatically determines $\alpha$, $i$, and $\beta$. The third option is the inclusion of a maneuver $\Delta V$ to better incorporate the perigee conditions before the multiple shooting algorithm is applied.

- To achieve a desirable flyby altitude, it is necessary to numerically correct the trajectory. A multiple shooting scheme supplies a robust algorithm for this task. A logical selection for the estimate of the $\Delta V$ location to update the perigee conditions is the apogee of the extended

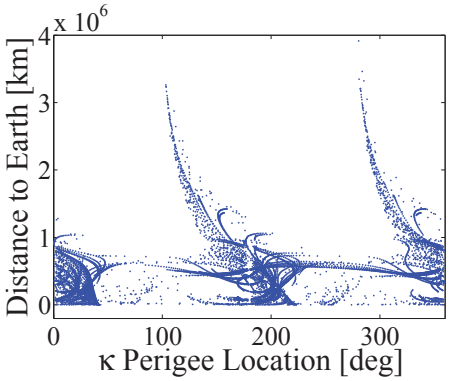


Figure 15: Perigee Conditions

Earth-Moon manifold trajectory. In fact, the $\Delta V$ location varies by only slightly during the numerical corrections process. In Figure 16, the near-Earth views of an Earth-Moon manifold transfer are plotted. The apogee maneuver location is indicated as $\Delta V_1$.

- The second $\Delta V$ is applied at the corrected perigee location for departure to Mars. A departure $\Delta V$ is estimated by computing a Hohmann transfer arc. Since the spacecraft is very near the Earth, it is convenient to calculate a $V_\infty$ value and use the two-body energy equation to estimate the $\Delta V$ at the perigee.

- When a transfer trajectory is computed, it is necessary to verify the location of Mars corresponding to the specified time-of-flight. The best possible arrival date is determined by identifying the best arrival conditions at Mars from a set of the possible locations. The potential arrival dates do not necessarily supply the desirable target location. Thus, the initial date requires modification to improve Mars' location at arrival. This modification obviously shifts the orientation of the Earth-Moon system, and results in a change in the flyby conditions at perigee. To minimize the change, the departure date is varied by increments, each approximately 29.5 days, i.e., the lunar synodic period. Thus, the Moon remains approximately at the same location in the Sun-Earth frame.

- After one possible Mars' arrival location is determined, additional potential final Mars' locations are identified by varying the final time with

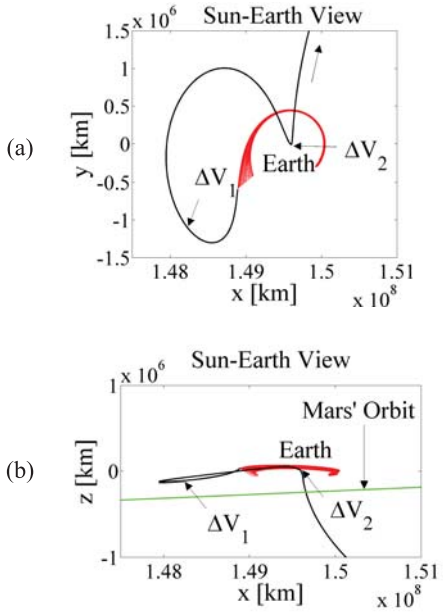


Figure 16: Earth-Moon Manifold Transfer from Earth-Moon $L_2$: Views near the Earth

the step size corresponding to Mars' synodic period which is approximately 780 days.

- Generally, additional $\Delta V$ locations lower the total $\Delta V$ requirements. A suggested initial guess for an additional maneuver location is the maximum $y$-excursion along the transfer path. The final location of the maneuver after the numerical corrections process tends to remain close to this region even without a location constraint as demonstrated in Figure 17.

- In this transfer scenario, the transfer arc associated with a Hohmann transfer is not a sufficiently accurate approximation to serve as an adequate initial guess. The initial guess can be improved by adjusting the $\Delta V$ before the multiple shooting procedure is applied.

The results from these sample cases appear in Table 3. The EM$Az$ amplitude is $25,000$ km. The departure opportunity recurs every two years. The time spent near Earth until the second maneuver is approximately 160 days because of the low energy dynamics associated with the manifold trajectories. The flyby altitude is selected to be equal to $1,000$ km. The resulting

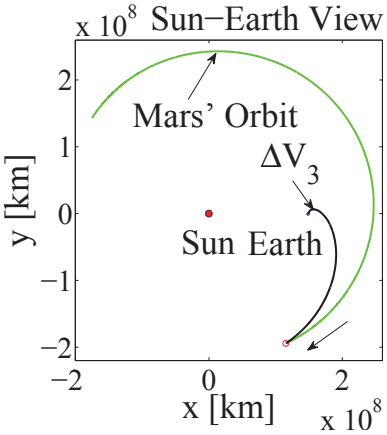


Figure 17: Earth-Moon Manifold Transfer from Earth-Moon $L_2$: The location of the third maneuver is indicated by $\Delta V_3$.

total $\Delta V$ is significantly lower than the first scenario via Sun-Earth manifold trajectories. However, the total time of flight is $100 - 200$ days longer than in the first scenario.

Similar guidelines apply to EM manifold transfers from EM$L_1$ halo orbits. In this case, unstable EM manifold trajectories are propagated toward the Moon to escape to the exterior region as demonstrated in Figure 18(a). This type of transfer, exploiting the exterior region, is defined as an exterior transfer. The general transfer paths are similar to the transfers from the $L_2$ side as displayed in Figure 18(b); sample results are listed in Table 3. As in the $L_2$ examples, the time spent prior to the second maneuver is approximately 160 days. For transfers from the $L_1$ side, an additional scenario is considered where unstable EM manifold trajectories are propagated towards the interior region. A sample trajectory arc originating from an EM$L_1$ halo orbit in the Earth-Moon rotating frame appears in Figure 19(a). This transfer type, exploiting the interior region, is defined as an interior transfer. In the figure, an unstable manifold arc is plotted in red. Two maneuvers are applied to target an desired Earth flyby. The first maneuver occurs at a perigee and the second at an apogee. A sample trajectory arc in the Sun-Earth rotating frame is displayed in Figure 19(b). Results from sample cases for the $L_1$ interior transfers appear in Table 4. Generally, the time-of-flight values are lower, but total $\Delta V$ values are higher than in exterior transfer cases.

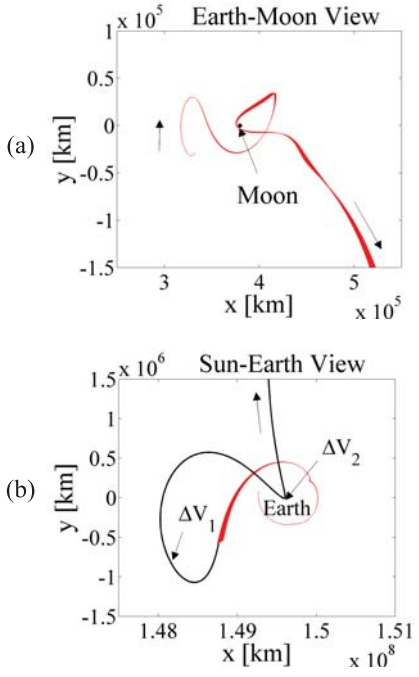


Figure 18: Earth-Moon $L_1$ Manifold Exterior Transfer from Earth-Moon $L_1$: Unstable manifold trajectories propagated towards the exterior region

*6.3. Direct Transfers*

The third scenario involves direct transfers that do not exploit manifolds. In this example, a maneuver is applied to depart an EM$L_2$ halo orbit and target a close flyby at the Earth. In Figure 20, a departure trajectory in an Earth-Moon view is plotted in red. Since this scenario does not exploit manifolds, the time-of-flight is reduced significantly. However, the direct transfer requires a significant level of $\Delta V$ to depart an EM$L_2$ halo orbit. The corresponding guidelines are:

- In the departure EM halo orbit, a maneuver is introduced at the location where the $y$-component is zero and the $z$-component is a maximum, as indicated in Figure 20. This maneuver allows the spacecraft to move along a trajectory arc and pass close to the Earth. The magnitude of the $\Delta V$ is adjusted to achieve a desired perigee altitude.

- The propagated trajectory is transformed into the Sun-Earth frame by use of the phase angles, $\alpha$, $i$, and $\beta$. The direct transfers offer more

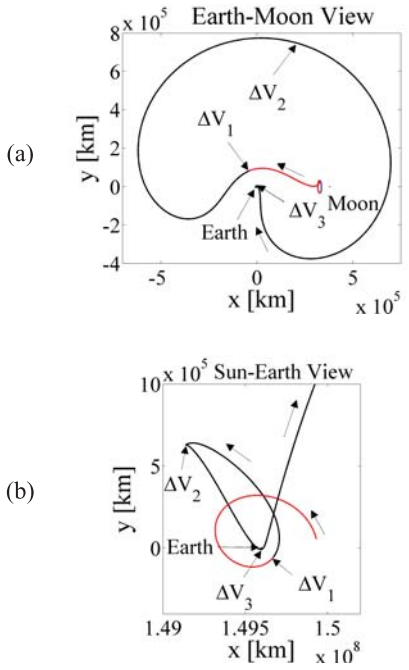


Figure 19: Earth-Moon $L_1$ Manifold Interior Transfer from Earth-Moon $L_1$: An unstable manifold trajectory propagated towards the interior region

flexibility in selecting values of $\alpha$ and $\beta$ than other scenarios. The angles (i.e., the location of the Moon in its orbit) are selected such that the perigee occurs in the fourth quadrant in the Sun-Earth frame for promising flyby conditions. In Figure 21(a), the $x$-$y$ projection of the transformed path appears in red.

- The process to compute the transfer trajectory from the Earth flyby to Mars is the same as the procedure in the second scenario.

The results from the sample cases are summarized in Table 5. The EM$Az$ value is specified as $25,000$ km. This scenario delivers spacecraft to Mars in a significantly shorter time than the second scenario. In Figure 21(a), the gray arc represents the trajectory originally computed in the Earth-Moon system, as displayed in Figure 20. The time-of-flight along the arc is only about 6 days. However, the $\Delta V$ cost is higher due to the fact that the maneuver to depart the EM halo orbit is larger. Approximately 925 m/sec is required to depart a halo orbit and reach a suitable perigee point, i.e., $1,000$ km altitude at Earth passage.

Table 3: Earth-Moon $L_2$ Manifold and $L_1$ Manifold Exterior Transfers: EM$Az$ = 25,000 km; Leg 1 is from the departure from EM halo to $\Delta V_1$. Leg 2 is from $\Delta V_1$ to $\Delta V_2$. Leg 3 is from $\Delta V_2$ to $\Delta V_3$.

| Departure Date: | | Leg 1 | Leg 2 | Leg 3 | Total |
|---|---|---|---|---|---|
| EM$L_2$ Departure | | | | | |
| May 28, 2026 | TOF [days] | 75 | 90 | 35 | 424 |
| | $\Delta V$ [km/sec] | 0.020 | 0.570 | 0.331 | 0.921 |
| July 3, 2028 | TOF [days] | 75 | 77 | 45 | 380 |
| | $\Delta V$ [km/sec] | 0.003 | 0.450 | 0.307 | 0.759 |
| October 7, 2030 | TOF [days] | 80 | 71 | 46 | 467 |
| | $\Delta V$ [km/sec] | 0.046 | 0.515 | 0.684 | 1.245 |
| EM$L_1$ Exterior Departure | | | | | |
| May 16, 2026 | TOF [days] | 89 | 73 | 41 | 441 |
| | $\Delta V$ [km/sec] | 0.006 | 0.391 | 0.500 | 0.897 |
| June 21, 2028 | TOF [days] | 90 | 69 | 50 | 388 |
| | $\Delta V$ [km/sec] | 0.030 | 0.517 | 0.254 | 0.802 |
| September 26, 2030 | TOF [days] | 90 | 71 | 46 | 487 |
| | $\Delta V$ [km/sec] | 0.020 | 0.463 | 0.207 | 0.690 |

Table 4: Earth-Moon $L_1$ Manifold Interior Transfer: EM$Az$ = 25,000 km; Leg 1 is from the departure from EM halo to $\Delta V_1$. Leg 2 is from $\Delta V_1$ to $\Delta V_2$. Leg 3 is from $\Delta V_2$ to $\Delta V_3$. Leg 4 is from $\Delta V_3$ to $\Delta V_4$.

| Departure Date: | | Leg 1 | Leg 2 | Leg 3 | Leg 4 | Total |
|---|---|---|---|---|---|---|
| EM$L_1$ Interior | | | | | | |
| September 27, 2026 | TOF [days] | 16 | 17 | 14 | 37 | 318 |
| | $\Delta V$ [km/sec] | 0.200 | 0.252 | 0.583 | 0.166 | 1.201 |
| November 03, 2028 | TOF [days] | 16 | 17 | 14 | 36 | 266 |
| | $\Delta V$ [km/sec] | 0.200 | 0.252 | 0.555 | 0.499 | 1.505 |
| November 03, 2028 | TOF [days] | 16 | 17 | 14 | 36 | 252 |
| | $\Delta V$ [km/sec] | 0.200 | 0.252 | 0.367 | 0.701 | 1.520 |

Similar guidelines apply to produce transfers from $L_1$ halo orbits. A generally successful location for placement of the first maneuver to depart an $L_1$ halo orbit also occurs where the $y$-component is zero, but the $z$-component is a minimum as plotted in Figure 22. The size of the $\Delta V$ is still significant, e.g., 575 m/sec to depart an $L_1$ halo orbit corresponding to an amplitude of 25,000 km $Az$, as noted in Table 5.

### *6.4. Transfers with Lunar Flyby*

The fourth scenario is a transfer that exploits manifolds as well as a lunar flyby. Instead of applying a maneuver to depart an $L_2$ halo orbit and constructing Earth flyby conditions, a maneuver is applied at perilune along an unstable EM manifold trajectory, one that is approaching the Moon, to produce Earth flyby conditions. Once the Earth flyby conditions are achieved, the guidelines are the same as the third scenario for direct transfers. The time-of-flight from an $L_2$ halo orbit to Earth is approximately 20 days

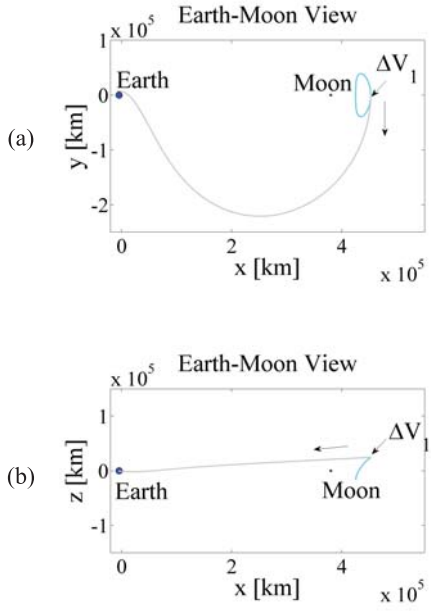


Figure 20: Direct Transfer from Earth-Moon $L_2$: $\Delta V$ is applied to leave a halo orbit.

for the sample results in Table 6. Note that the selected EM$Az$ is $5,000$ km. The value of the $\Delta V$ at the lunar flyby increases as a function of the EM$Az$. However, an additional maneuver to depart a halo orbit reduces the amount of $\Delta V$ to achieve the Earth flyby for larger halo orbits [42]. A sample trajectory with a departure maneuver appears in Figure 23. The departure along the gray trajectory appears smooth in the $x$-$y$ projection, Figure 23(a), but not in the $x$-$z$ projection, Figure 23(b). The maneuver, $\Delta V_1$, primarily adjusts the velocity in the $z$ direction to achieve a lunar flyby at a 100-km altitude. A similar scenario is constructed to depart from EM$L_1$ halo orbits. The gray trajectory departs an $L_1$ halo orbit with a seemingly sharp change in direction in Figures 24(a)-(b), a shift reflected in the $\Delta V$. As predicted, the departure maneuver $\Delta V_1$ is higher in $L_1$ cases as summarized in Table 7. The total maneuver to achieve the Earth flyby from the EM$L_2$ orbit and EM$L_1$ orbit are 329 m/sec and 500 m/sec, respectively. However, in both cases, the maneuver value is reduced from the direct examples, e.g., 925 m/sec for the $L_2$ departure and 575 m/sec for the $L_1$ departure.

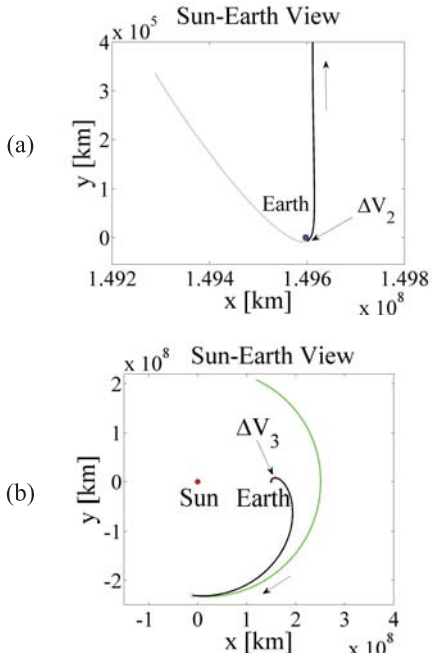


Figure 21: Direct Transfer from Earth-Moon $L_2$: Two additional $\Delta V$s are applied to reach Mars.

### *6.5. Transition to Higher-Fidelity Model*

To evaluate the functionality of the blended model, results from each transfer scenario are transitioned to a higher-fidelity model with ephemeris positions of Sun, Earth, Moon, and Mars. Sample results from the ephemeris model are listed in Table 8. Departure dates predicted from the blended model are reasonable estimates for use in the ephemeris model. Also, time-of-flight values are estimated quite well by the blended model. The total $\Delta V$ values generally increase after the transition, but the increases are within a few hundred m/sec. Sample results from an $L_1$ transfer scenario with a lunar flyby are displayed in Figure 25; the path originates from an EM$L_1$ halo orbit. The original EM halo orbit is in cyan, and the transfer path is plotted in gray in Figures 25(a)-(b). The trajectory in the ephemeris model is plotted in magenta. The results in the eleventh and twelfth rows in Table 8 indicate that the EM$Az$ increases from $25,000$ km to $29,000$ km after the transition to the ephemeris model. However, the gray path is a good estimate and the magenta trajectory appears to possess similar characteristics. In Figure 25(c), the trajectory from the blended model is plotted in black, and the

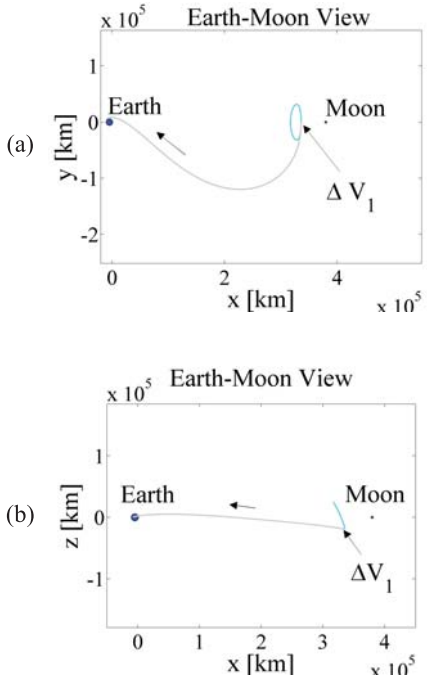


Figure 22: Direct Transfer from Earth-Moon $L_1$: $\Delta V$ is applied to leave a halo orbit.

trajectory from the ephemeris model is plotted in magenta in the Sun-Earth rotating frame. The magenta trajectory follows a path similar to the black path.

## 7. CONCLUSIONS

General design procedures for four transfer scenarios from Earth-Moon $L_1/L_2$ halo orbits to Mars are developed. In addition, to exploit Sun-Earth manifolds as an option for transfers to Mars, a general procedure to compute maneuver-free transfers between Earth-Moon $L_2$ halo orbits to Sun-Earth $L_2$ halo orbits is described. This procedure is sufficiently general to support the construction of maneuver-free transfers between Earth-Moon $L_2$ halo orbits from/to Sun-Earth $L_1/L_2$ halo orbits. The model of a five-body regime in which gravitational bodies are Sun, Earth, Moon, and Mars is constructed by blending Earth-Moon and Sun-Earth systems with the ephemeris Mars location. Then, the results produced in the blended model are transitioned to a higher-fidelity model with ephemeris Sun, Earth, Moon, and Mars locations.

Table 5: Direct Transfers: EM$Az = 25{,}000$ km; Leg 1 is from the departure from EM halo to the Earth flyby. Leg 2 is from the Earth flyby to $\Delta V_3$. Leg 3 is from $\Delta V_3$ to Mars.

| Departure Date: | | Leg 1 | Leg 2 | Leg 3 | Total |
|---|---|---|---|---|---|
| EM$L_2$ Departure | | | | | |
| November 4, 2026 | TOF [days] | 6 | 38 | 228 | 272 |
| | $\Delta V$ [km/sec] | 0.925 | 0.581 | 0.088 | 1.593 |
| December 11, 2028 | TOF [days] | 6 | 38 | 162 | 206 |
| | $\Delta V$ [km/sec] | 0.925 | 0.580 | 0.130 | 1.635 |
| March 18, 2031 | TOF [days] | 6 | 37 | 300 | 343 |
| | $\Delta V$ [km/sec] | 0.925 | 0.512 | 0.013 | 1.450 |
| EM$L_1$ Departure | | | | | |
| November 4, 2026 | TOF [days] | 5 | 39 | 234 | 277 |
| | $\Delta V$ [km/sec] | 0.575 | 0.591 | 0.049 | 1.215 |
| December 11, 2028 | TOF [days] | 5 | 40 | 182 | 226 |
| | $\Delta V$ [km/sec] | 0.575 | 0.631 | 0.217 | 1.423 |
| January 18, 2031 | TOF [days] | 5 | 38 | 150 | 193 |
| | $\Delta V$ [km/sec] | 0.575 | 0.450 | 0.550 | 1.575 |

Table 6: EM $L_2$ Manifold Transfers with Lunar Flyby: EM$Az = 5{,}000$ km; Leg 1 is from the departure from EM$L_2$ to the Earth flyby. Leg 2 is from the Earth flyby to $\Delta V_3$. Leg 3 is from $\Delta V_3$ to Mars.

| Departure Date: | | Leg 1 | Leg 2 | Leg 3 | Total |
|---|---|---|---|---|---|
| October 21, 2026 | TOF [days] | 20 | 39 | 233 | 292 |
| | $\Delta V$ [km/sec] | 0.236 | 0.612 | 0.074 | 0.923 |
| November 26, 2028 | TOF [days] | 20 | 39 | 195 | 253 |
| | $\Delta V$ [km/sec] | 0.236 | 0.590 | 0.165 | 0.991 |
| January 3, 2031 | TOF [days] | 20 | 38 | 160 | 218 |
| | $\Delta V$ [km/sec] | 0.236 | 0.416 | 0.591 | 1.243 |

The comparison of the results demonstrates that the trajectories computed from the blended model produce a reasonable guess to be transitioned to the ephemeris model.

## 8. ACKNOWLEDGEMENTS

The authors appreciate the support from the School of Aeronautics and Astronautics as well as the School of Engineering Education. Portions of the work were also completed under NASA Grant Nos. NNX13AE55G and NNX13AH02G.

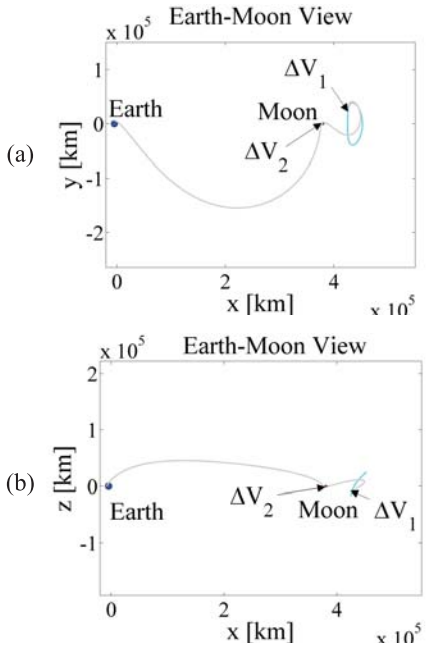


Figure 23: Transfer with Lunar Flyby from Earth-Moon $L_2$: $\Delta V_1$ is applied to leave a halo orbit. $\Delta V_2$ is applied at a perilune.

Table 7: $L_1$ and $L_2$ Direct Transfers with Lunar Flyby: EM$Az$ = 25,000 km; Leg 1 is from the departure from EM halo to the lunar flyby. Leg 2 is from the lunar flyby to the Earth flyby. Leg 3 is from the Earth flyby to $\Delta V_4$. Leg 4 is from $\Delta V_4$ to Mars.

| Departure Date: | | Leg 1 | Leg 2 | Leg 3 | Leg 4 | Total |
|---|---|---|---|---|---|---|
| EM$L_2$ Departure | | | | | | |
| October 25, 2026 | TOF [days] | 10 | 5 | 39 | 230 | 284 |
| | $\Delta V$ [km/sec] | 0.079 | 0.250 | 0.650 | 0.102 | 1.082 |
| December 1, 2028 | TOF [days] | 10 | 5 | 40 | 195 | 249 |
| | $\Delta V$ [km/sec] | 0.079 | 0.250 | 0.666 | 0.155 | 1.150 |
| January 7, 2031 | TOF [days] | 10 | 5 | 40 | 148 | 202 |
| | $\Delta V$ [km/sec] | 0.079 | 0.250 | 0.487 | 0.557 | 1.373 |
| EM$L_1$ Departure | | | | | | |
| November 2, 2026 | TOF [days] | 2 | 3 | 34 | 231 | 271 |
| | $\Delta V$ [km/sec] | 0.230 | 0.270 | 0.495 | 0.324 | 1.319 |
| December 9, 2028 | TOF [days] | 2 | 3 | 35 | 175 | 215 |
| | $\Delta V$ [km/sec] | 0.230 | 0.270 | 0.498 | 0.260 | 1.258 |
| January 16, 2031 | TOF [days] | 2 | 3 | 36 | 170 | 210 |
| | $\Delta V$ [km/sec] | 0.230 | 0.270 | 0.304 | 1.038 | 1.842 |

(a)

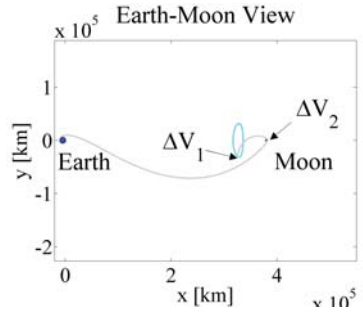


(b)

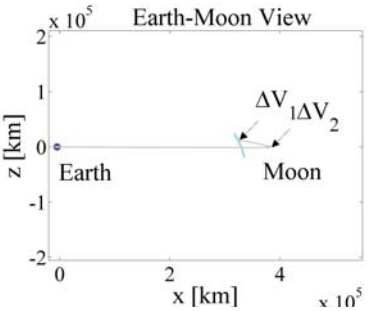


Figure 24: Transfer with Lunar Flyby from Earth-Moon $L_1$: $\Delta V_1$ is applied to leave a halo orbit. $\Delta V_2$ is applied at a perilune.

Table 8: Comparison of Results, Blended Model and Ephemeris: EMAz for the ephemeris case is the mean of maximum Az values of the quasi-halo orbit. (*: direct case with an additional maneuver)

| | Case | EMAz [km] | Departure Date | TOF [day] | $\Delta V$ [km/sec] |
|---|---|---|---|---|---|
| 1 | SE Transfer Blended | 25,000 | June 16, 2022 | 350 | 3.495 |
| 2 | SE Transfer Ephemeris | 25,000 | June 16, 2022 | 350 | 3.645 |
| 3 | $L_2$ EM Blended | 25,000 | July 3, 2028 | 380 | 0.759 |
| 4 | $L_2$ EM Ephemeris | 23,000 | July 3, 2028 | 377 | 0.850 |
| 5 | $L_1$ EM Ext. Blended | 25,000 | June 21, 2028 | 388 | 0.802 |
| 6 | $L_1$ EM Ext. Ephemeris | 24,000 | June 21, 2028 | 388 | 0.997 |
| 7 | $L_1$ EM Int. Blended | 25,000 | November 3, 2028 | 266 | 1.505 |
| 8 | $L_1$ EM Int. Ephemeris | 24,000 | November 3, 2028 | 267 | 1.731 |
| 9 | $L_2$ Direct Blended | 25,000 | December 11, 2028 | 257 | 2.235 |
| 10 | $L_2$ Direct Ephemeris | 25,000 | December 11, 2028 | 248 | 2.568 |
| 11 | $L_1$ Direct Blended | 25,000 | December 4, 2028 | 226 | 1.423 |
| 12 | $L_1$ Direct Ephemeris | 29,000 | December 4, 2028 | 214 | 1.615 |
| 13 | $L_2$ Lunar Blended | 5,000 | November 26, 2028 | 253 | 0.991 |
| 14 | $L_2$ Lunar Ephemeris | 6,000 | November 26, 2028 | 250 | 1.096 |
| 15 | $L_2$ Lunar* Blended | 25,000 | December 1, 2028 | 249 | 1.150 |
| 16 | $L_2$ Lunar* Ephemeris | 27,000 | December 1, 2028 | 249 | 1.413 |
| 17 | $L_1$ Lunar* Blended | 25,000 | December 9, 2028 | 215 | 1.258 |
| 18 | $L_1$ Lunar* Ephemeris | 29,000 | December 9, 2028 | 212 | 1.415 |

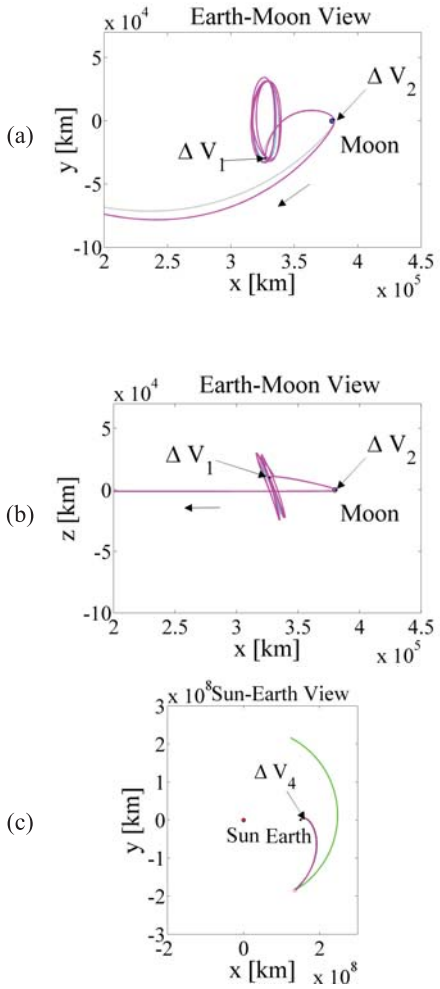


Figure 25: Direct Transfer with a Lunar Flyby from EM $L_1$ Halo Orbit: EMAz = 25,000 km. The departure date is December 9, 2028. The trajectory in the ephemeris model is plotted in magenta.

## References


[1] R. W. Farquhar, The Utilization of Halo Orbits in Advanced Lunar Operations, NASA Technical Note, NASA TN D-6365, 1971.

[2] M. Woodard, D. Folta, and D. Woodfork, ARTEMIS: The First Mission to the Lunar Libration Points, 21st International Symposium on Space Flight Dynamics, Toulouse, France, September 28 - October 2 2009.

[3] J. Hopkins, Fastnet: Early Telerobotic Exploration of the Lunar Farside by Astronauts at Earth-Moon $L_2$, Future In-Space Operations colloquium, November 14 2012.

[4] K. C. Howell, B. T. Barden, and M. W. Lo, Application of Dynamical Systems Theory to Trajectory Design for a Libration Point Mission, The Journal of the Astronautical Sciences, vol. 45, pp. 161–178, April-June 1997.

[5] D. Burnett, B. Barraclough, R. Bennet, M. Neugebauer, L. Oldham, C. Sasaki, D. Sevilla, N. Smith, E. Stansbery, D. Sweetnam, R. Wiens, The Genesis Discovery Mission: Return of Solar Matter to Earth, Space Science Reviews, vol. 105, pp. 509–534, 2003.

[6] K. Howell, B. Barden, R. Wilson, and M. Lo, Trajectory Design Using a Dynamical Systems Approach with Application to Genesis, Paper No. AAS 97-709, AIAA/AAS Astrodynamics Specialist Conference, Sun Valley, Idaho, August 1997.

[7] M. W. Lo, B. G. Williams, W. E. Bollman, D. Han, R. A. Corwin, P. E. Hong, K. C. Howell, B. Brian, and R. Wilson, Genesis Mission Design, Paper No. AIAA-1998-4468, AIAA/AAS Astrodynamics Specialist Conference and Exhibit, Boston, Massachusetts, August 1998.

[8] D. Folta and K. Richon, Libration Orbit Mission Design at L2: A Map and NGST Perspective, Paper No. AIAA 98-4469, AIAA/AAS Astrodynamics Specialist Conference, Boston, MA, August 10-12 1998.

[9] H. Franz, P. Sharer, K. Ogilvie, and M. Desch, WIND Nominal Mission Performance and Extended Mission Design, Journal of the Astronautical Sciences, vol. 49, pp. 145–167, 2001.

[10] G. Gómez, W. Koon, M. Lo, J. Marsden, S. Ross, and J. Masdemont, Invariant Manifolds, the Spatial Three-Body Problem and Petit Grand Tour of Jovian Moons, Libration Point Orbits and Application, pp. 587–601, 2003.

[11] G. Gómez, W. Koon, M. Lo, J. Marsden, J. Masdemont, and S. Ross, Connecting Orbits and Invariant Manifolds in the Spatial Restricted Three-Body Problem, Nonlinearity, vol. 17, no. 5, p. 1571, 2004.

[12] W. S. Koon, M. W. Lo, J. E. Marsden, and S. D. Ross, Constructing a Low Energy Transfer between Jovian Moons, Contemporary Mathematics, pp. 129–145, 2002.

[13] W. S. Koon, M. W. Lo, J. E. Marsden, and S. D. Ross, Shoot the Moon, Paper No. AAS 00-166, AAS/AIAA Space Flight Mechanics Meeting, Clearwater, Florida, January 2000.

[14] W. S. Koon, M. W. Lo, J. E. Marsden, and S. D. Ross, Low Energy Transfer to The Moon, Celestial Mechanics and Dynamical Astronomy, pp. 63–73, 2001.

[15] J. Parker and M. Lo, Shoot the Moon 3D, Paper No. AAS 05-383, AAS/AIAA Astrodynamics Specialists Conference, Lake Tahoe, California, August 2005.

[16] J. Parker, Families of Low Energy Lunar Halo Transfers, Paper No. AAS 06-132, AAS/AIAA Spaceflight Mechanics Meeting, Tampa, Florida, January 2006.

[17] J. S. Parker and G. H. Born, Modeling a Low-Energy Ballistic Lunar Transfer Using Dynamical Systems Theory, Journal of Spacecraft and Rockets, vol. 45, no. 6, pp. 1269–1281, 2008.

[18] J. Parker, Low-Energy Ballistic Transfers to Lunar Halo Orbits, Paper No. AAS 09-443, AAS/AIAA Astrodynamics Specialist Conference, Pittsburgh, Pennsylvania, August 2009.

[19] K. C. Howell and M. Kakoi, Transfers between the Earth-Moon and Sun-Earth Systems Using Manifolds and Transit Orbits, Acta Astronautica, vol. 59, pp. 367–380, 2006.

[20] E. Canalias and J. Masdemont, Computing Natural Transfers between Sun-Earth and Earth-Moon Lissajous Libration Point Orbits, Acta Astronautica, vol. 63, pp. 238–248, 2008.

[21] K. Howell, M. Beckman, C. Patterson, and D. Folta, Representations of Invariant Manifolds for Applications in Three-Body Systems, The Journal of the Astronautical Sciences, vol. 54, no. 1, pp. 69–93, 2006.

[22] G. Mingotti, F. Topputo, and F. B. Zazzera, Attainable Sets in Space Mission Design: a Method to Define Low-Thrust, Invariant Manifold Trajectories, Paper No. AAS-12-137, AAS/AIAA Space Flight Mechanics Meeting,Charleston,South Carolina, January 2012.

[23] P. Zhang, J. Li, H. Baoyin, and G. Tang, A Low-Thrust Transfer between the Earth-Moon and Sun-Earth Systems Based on Invariant Manifolds, Acta Astronautica, 2013.

[24] M. Lo and S. Ross, The Lunar $L_1$ Gateway: Portal to the Stars and Beyond, AIAA Space 2001 Conference and Exposition, Albuquerque, New Mexico, August 2001.

[25] M. W. Lo, The Interplanetary Superhighway and the Origins Program, IEEE Aerospace Conference Proceedings, vol. 7, pp. 3543–3562, March 9-16 2002.

[26] G. P. Alonso, The Design of System-To-System Transfer Arcs Using Invariant Manifolds in the Multi-Body Problem, Ph.D. Dissertation, School of Aeronautics and Astronautics, Purdue University, West Lafayette, Indiana, December 2006.

[27] F. Topputo, M. Vasile, and A. E. Finzi, An Approach to the Design of Low Energy Interplanetary Transfers Exploiting Invariant Manifolds of the Restricted Three-Body Problem, Paper No. AAS 04-245, AAS/AIAA Space Flight Mechanics Conference,Maui, Hawaii, February 2004.

[28] F. Topputo, M. Vasile, and F. B. Zazzera, A Hybrid Optimization of the Low Energy Interplanetary Transfers Associated to the Invariant Manifolds of the Restricted Three-Body Problem, Paper No. IAC-04-A.6.06, International Astronautical Congress, Vancouver, Canada, October 2004.

[29] M. Nakamiya, D. Scheeres, H. Yamakawa, and M. Yoshikawa, A Study of Earth–Mars Interplanetary Transfer Using Spaceports at the Lyapunov Orbits of Sun-Earth and Sun-Mars System, Paper No. IAC-08-A5.3.07, International Astronautical Congress, Glasgow, Scotland, October 2008.

[30] M. Nakamiya, H. Yamakawa, D. Sheeres, and M. Yoshikawa, Interplanetary Transfers between Halo Orbits: Connectivity between Escape and Capture Trajectories, Journal of Guidance, Control, and Dynamics, vol. 33, pp. 803–813, May-June, 2010.

[31] G. Mingotti and P. Gurfil, Mixed Low-Thrust and Invariant-Manifold Transfers to Unstable Distant Prograde Orbits around Mars, Paper No. AIAA 2010-7832, AAS/AIAA Astrodynamics Specialist Conference, Toronto, Ontario Canada, August 2010.

[32] G. Mingotti and F. Topputo and F. B. Zazzera, Invariant-Manifold, Low-Thrust Transfers to Low Mars Orbits, Paper No. IAC-10-C1.9.1, International Astronautical Congress, Prague, Czech Republic, September-October 2010.

[33] G. Mingotti, F. Topputo, and F. B. Zazzera, Earth-Mars Transfers with Ballistic Escape and Low-Thrust Capture, Celestial Mechanics and Dynamical Astronomy, vol. 110, pp. 169–188, June 2011.

[34] C. Finocchietti, P. Pergola, and M. Andrenucci, Venus Transfer Design by Combining Invariant Manifolds and Low–Thrust Arcs, Acta Astronautica, 2013.

[35] A. Haapala and K. Howell, Trajectory Design Strategies Applied to Temporary Comet Capture Including Poincaré Maps and Invariant Manifolds, Celestial Mechanics and Dynamical Astronomy, pp. 1–25, 2013.

[36] D. C. Folta, M. A. Woodard, T. A. Pavlak, A. F. Haapala, and K. C. Howell, Earth-Moon Libration Point Orbit Stationkeeping: Theory, Modeling, and Operations, Acta Astronautica, vol. 94, no. 1, pp. 421–433, 2014

[37] J. E. Prussing and B. A. Conway, Orbital Mechanics. New York: Oxford University Press, first ed., 1993.

[38] J. Stoer and R. Bulirsch, Introduction to Numerical Analysis. New York: Springer-Verlag, 1980.

[39] T. A. Pavlak and K. C. Howell, Evolution of the Out-of-Plane Amplitude for Quasi-Periodic Trajectories in the Earth–Moon System, Acta Astronautica, vol. 81, no. 2, pp. 456–465, 2012.

[40] M. Vaquero and K. C. Howell, Design of Transfer Trajectories between Resonant Orbits in the Earth-Moon Restricted Problem, Acta Astronautica, vol. 94, no. 1, pp. 302–317, 2014.

[41] T. A. Pavlak, Trajectory Design and Orbit Maintenance Strategies in Multi-Body Dynamical Regimes, Ph.D. Dissertation, School of Aeronautics and Astronautics, Purdue University, West Lafayette, Indiana, May 2013.

[42] D. Folta, T. Pavlak, A. Haapala, and K. Howell, Preliminary Considerations for Access and Operations in Earth-Moon L1/L2 Orbits, Paper No. AAS 13-339, AAS/AIAA Space Flight Mechanics Meeting, Kauai, Hawaii, February 10-14 2013.